

# On the Discrimination of Radar Signatures of Atmospheric Gravity Waves and Oceanic Internal Waves on Synthetic Aperture Radar Images of the Sea Surface

Werner Alpers, *Senior Member, IEEE*, and Weigen Huang

**Abstract**—Synthetic aperture radar (SAR) images acquired over the ocean frequently show sea wave-like patterns that have wavelengths well above those of ocean surface waves and that are sea surface signatures of oceanic internal waves (OIWs) or of atmospheric gravity waves (AGWs). However, it is often difficult to decide whether they result from the first or the second kind of waves, which has led many investigators to misinterpret SAR images of the sea surface. Based on solitary wave and radar imaging theories of AGWs and OIWs, we present criteria that help distinguish between them. However, there are cases where these criteria, which are based solely on the shape and structure of the features visible on the SAR images, yield ambiguous results. In these cases, one must resort to additional information on the generation of AGWs and OIWs, which are listed in this paper.

**Index Terms**—Atmospheric gravity waves (AGWs), internal waves, synthetic aperture radar (SAR).

## I. INTRODUCTION

ATMOSPHERIC gravity waves (AGWs) and oceanic internal waves (OIWs) are ubiquitous phenomena in the atmosphere and in the ocean, respectively. Most often, however, they have small amplitudes that make it difficult to identify them in data records. However, exceptions are large-amplitude nonlinear AGWs and OIWs that appear in wave groups and that are often described in terms of solitary wave theory.

Large-amplitude nonlinear AGWs are encountered in the troposphere as well as in the mesosphere [1], [2]. When generated in the troposphere, they can propagate upward or remain in the troposphere and get trapped there [3]–[6]. Observers on the ground occasionally can visualize these AGWs by cloud

patterns that sometimes show up in the lee of mountains [7]. These AGWs are called lee waves and usually consist of several cloud bands oriented parallel to the mountain range. They are formed when the moisture content of the air is sufficiently high and when the crests of the AGWs reach the condensation level. Spectacular cloud bands generated by solitary AGWs are observed in the southern part of the Gulf of Carpentaria in northern Australia where they have received considerable attention [2], [8], [9]. There, they usually appear early in the morning, which is why they are called “Morning Glories.” The Morning Glory is a dramatic cloud event consisting of a traveling low-level roll cloud or a series of roll clouds (often only 100–200 m high), which have typical widths between 1 and 2 km and are 1 km deep. They may extend in length for more than 100 km.

The visibility of the AGWs in the cloud pattern depends on the moisture content of the atmosphere. If the moisture content is insufficient, then no clouds are formed. However, in this case, the Morning Glory can still be detected by synthetic aperture radar (SAR) by the fingerprint that it leaves on the sea surface. To our knowledge, no spaceborne SAR images showing sea surface signatures of Morning Glories have been published so far. In this paper, we show two SAR images acquired by Envisat Advanced SAR (ASAR) showing this phenomenon.

AGWs propagating in the marine boundary layer which touch the sea surface become visible on SAR images by the variations that they cause in the sea surface roughness [10]–[18]. AGWs that propagate in the lower atmosphere layer are associated with a spatially variable near-surface wind (or, more precisely, with a variable wind stress), which modulates the short-scale sea surface roughness and, thus, via Bragg scattering, the backscattered radar power or the normalized radar cross section (NRCS). This modulation of the sea surface roughness generates the sea surface signature of AGWs and the associated modulation of the NRCS.

Unfortunately, not only variable wind stress associated with AGWs modulates the sea surface roughness and gives rise to wave patterns on the SAR image, but also variable surface currents associated with oceanic phenomena, like OIWs and tidal flow over periodic sandbanks. The strength of the sea surface roughness modulation caused by these oceanic phenomena has often the same magnitude as the surface roughness

Manuscript received December 3, 2009; revised March 11, 2010; accepted May 9, 2010. Date of publication October 18, 2010; date of current version February 25, 2011. This work was supported in part by the European Space Agency–Ministry of Science and Technology Dragon 2 Program under Project ID 5316 and in part by the Chinese Offshore Investigation and Assessment Program under Project ID 908-01-BC04.

W. Alpers was with State Key Laboratory of Satellite Ocean Environment Dynamics, Second Institute of Oceanography, State Oceanic Administration, Hangzhou 310012, China. He is now with the Centre for Marine and Atmospheric Sciences (ZMAW), Institute of Oceanography, University of Hamburg, 20146 Hamburg, Germany (e-mail: alpers@ifm.uni-hamburg.de).

W. Huang is with the State Key Laboratory of Satellite Ocean Environment Dynamics, Second Institute of Oceanography, State Oceanic Administration, Hangzhou 310012, China (e-mail: wghuang@mail.hz.zj.cn).

Digital Object Identifier 10.1109/TGRS.2010.2072930

modulation caused by AGWs. Furthermore, their spatial scales are often similar. Therefore, it is difficult to identify unambiguously wave-like patterns visible on SAR images of the sea surface as radar signatures of AGWs, OIW<sub>s</sub>, or sandbanks. Determining which phenomenon causes the sea surface signature visible on the SAR image usually involves several criteria. We will show in this paper that there exist some characteristic differences in the radar signatures that in many cases are sufficient to discriminate between nonlinear AGWs and OIW<sub>s</sub>, which often appear in wave packets. These signatures follow from previously developed theories of SAR imaging mechanisms of AGWs and OIW<sub>s</sub> (see, e.g., [11] and [19]–[22]).

Large-amplitude nonlinear OIW<sub>s</sub> are encountered when the ocean is stratified, i.e., when the water density varies with depth and when strong currents (usually of tidal origin) interact with shallow underwater bottom topography. When the tide pushes the stratified water column over, for example, a shallow underwater ridge, it induces a disturbance in the water column from which solitary OIW<sub>s</sub> may evolve. Prominent areas that are birth places of large-amplitude solitary OIW<sub>s</sub> are the Straits of Gibraltar and Messina in the Mediterranean Sea [23]–[30], the Lombok Strait between the Indonesian islands Bali and Lombok [31], the Luzon Strait between Luzon and Taiwan [32]–[34], the sills in the Sulu Archipelago around Pearl Bank [35], [36], the shallow sea areas between the Andaman and Nicobar Islands, and the northwest coast of Sumatra in the eastern Indian Ocean [37]–[40]. Nonlinear OIW<sub>s</sub> are also frequently encountered in upwelling regions, e.g., north of Taiwan.

Sea surface signatures of OIW<sub>s</sub> have been detected on spaceborne SAR images as early as 1978 in SAR images acquired by the American Seasat satellite. At that time, the oceanographic community was quite surprised to see that OIW<sub>s</sub> could generate such large sea surface signatures. The wave patterns visible on the SAR images could easily be associated with OIW<sub>s</sub> because they were located in sea areas where internal waves were known to exist. An exception was the Seasat SAR image acquired on September 18, 1978, over the Mediterranean Sea on which a wave pattern was visible north of the Strait of Messina [23]. At that time, it was not known that internal waves could be generated at the Strait of Messina, but later, *in situ* measurements have confirmed it [25], [41].

After 1991, when the first European Remote Sensing (ERS) satellite ERS-1 carrying a SAR was launched, spaceborne SAR images have been extensively used in OIW investigations over different regions of the world's oceans. These SAR images have been acquired by the European satellites ERS-1, ERS-2, and Envisat, the Canadian satellites Radarsat-1 and Radarsat-2, the Japanese ALOS satellite (Advanced Land Observing Satellite), the German satellite TerraSAR-X, and the Italian COSMOS-Skymed (Constellation of small Satellites for Mediterranean basin Observation) satellites. So far, the most systematic study on the global distribution of OIW<sub>s</sub> using spaceborne images acquired in the microwave (radar), infrared, and visible bands was carried out by Global Oceans Associates. They have published "An Atlas of Internal Solitary-like Waves and Their Properties," which is available on the Internet (<http://www.internalwaveatlas.com>).

## II. RADAR SIGNATURES OF AGWs

AGWs become visible on SAR images because they are associated with variations of the wind stress at the sea surface. The wind stress depends on the wind speed at the sea surface and the stability of the air–sea interface. Variations of the wind stress disturb the small-scale sea surface roughness and, thus, give rise to sea surface signatures visible on the SAR image as variations of the NRCS or SAR image intensity.

The function that relates the NRCS to the wind vector  $\mathbf{W}$  for a neutrally stable atmosphere at a height of 10 m above the sea surface are called wind scatterometer model functions. The ones that are most often used to retrieve near-sea surface wind speeds from NRCS data acquired by the SARs onboard the ERS and Envisat satellites are the "C-band Wind Scatterometer Model Function 4" (CMOD4) [42], the CMOD\_IFR2 model developed by IFREMER [43], and the CMOD5 model (<http://www.knmi.nl/scatterometer/cmmod5>). However, quantitative information on the sea surface wind speed can only be extracted from SAR images when the wind direction near the sea surface is known. The wind direction is sometimes inferred from the SAR images itself, e.g., from the direction of wind streaks or from the direction of wind shadows behind coastal mountains or mountainous islands [44]–[46]. Another way to obtain wind direction is from atmospheric models, like the one developed by the National Center for Environmental Prediction (NCEP) in the U.S.

According to most wind scatterometer models, the normalized radar cross section  $s$  for a wind field consisting of a background (ambient) and the AGW induced wind field is given by

$$\begin{aligned}\sigma &= \sigma_0 + \Delta\sigma \\ &= B(\theta)|W + \Delta W|^{\gamma(\theta)} \\ &\quad \times (1 + b(\theta, W + \Delta W) \cos(\Phi + \Delta\Phi) \\ &\quad + c(\theta, W + \Delta W) \cos 2(\Phi + \Delta\Phi))\end{aligned}\quad (1)$$

where  $\sigma$  denotes the total NRCS,  $\sigma_0$  denotes the NRCS of the background, and  $\Delta\sigma$  denotes the NRCS variation induced by the wind speed variation  $\Delta W$  associated with the AGW. The angle  $\Phi$  is the direction of the ambient wind relative to the look direction of the SAR antenna,  $\Delta\Phi$  is the variation in wind direction associated with the AGW, and  $\theta$  is the local incidence angle. The functions  $B(\theta)$ ,  $\gamma(\theta)$ ,  $b(\theta, W)$ , and  $c(\theta, W)$  are empirical functions that have been determined experimentally [42]. However, different authors use slightly different values in their models. Note that  $\gamma$ , which is also called the wind speed exponent, is a strong function of radar frequency. Its value is around 1.5 for C-band radars (like the one onboard the Envisat and ERS satellites), around 1.0 for L-band radars (like the ones onboard the Seasat and ALOS satellites), and around 2.0 for X-band radars (like the one onboard the TerraSAR-X satellite). This means that atmospheric features are better visible in C-band SAR images than on L-band SAR images, and even better visible on X-band SAR images.

When  $\Delta\Phi = 0$  or  $= 180^\circ$ , i.e., when the propagation direction of the AGW is antiparallel or parallel to the ambient wind direction, and when this direction is known, it is straightforward to extract the wind speed fluctuations  $\Delta W(\mathbf{x})$  associated with

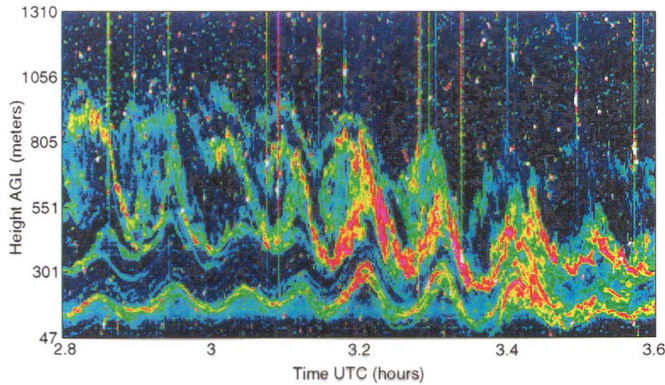


Fig. 1. Atmospheric gravity wave packet consisting of solitons of elevation measured by a zenith-pointing ground-based radar operating at a frequency of 2.9 GHz. The reflectivity pattern is caused by large temperature gradients associated with the isotherm density pattern (adapted from [48]).

the AGW from the SAR image using (1). This condition is usually fulfilled when the AGWs are generated by the interaction of air flow with coastal or island topography, but not when they are generated by atmospheric fronts [11]. In these cases, additional information on the direction of the local wind field is needed to extract variations of the near-surface wind speed from SAR images of the sea surface.

Large-amplitude nonlinear AGWs usually appear in wave packets consisting of one or several solitons [47]. However, unlike their oceanic counterparts, which are usually solitons of depression, the atmospheric solitons that touch the ocean surface are usually solitons of elevation. This has been confirmed by many measurements, among others by ground-based radar measurements. In Fig. 1, a radar record is depicted that shows the isotherm density pattern associated with a low-level nonlinear AGW passing over a site in New Mexico on October 20, 1992 (adapted from [48]). This record was acquired by a zenith-pointing frequency-modulated continuous wave radar operating at a frequency of 2.9 GHz. Visible are thin zones of strong backscatter (red and yellow color coded), which are associated with sharp gradients in air temperature.

The AGWs often observed behind mountains (lee waves) are usually also (weakly) nonlinear having troughs, which are much wider than the crests. Fig. 2 shows a schematic plot of the streamlines associated with a typical lee wave (adapted from [49]), where the asymmetric shape is apparent in the streamline pattern. Note that under the narrow wave crests, the streamlines are directed in the wave propagation direction and opposite to the direction into which the wind is blowing. Strongly nonlinear or solitary AGWs generated by the interactions of different air masses at atmospheric fronts have even more asymmetric shapes. This is depicted schematically in Fig. 3, where in the upper plot (a), an isoline of potential temperature (or air density) associated with a wave packet consisting of three solitons of elevation is shown. The arrows below the isoline denote the direction and the magnitude of the surface wind associated with these solitary AGWs. As in Fig. 2, this figure shows that the direction of the airflow is alternating at the sea surface: under the solitons of elevation this direction is antiparallel to the direction of the ambient airflow, while between the two solitons of elevation, it is directed parallel to

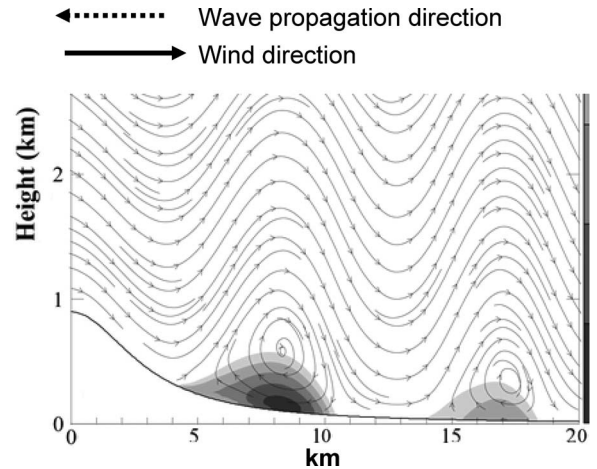


Fig. 2. Streamlines associated with a nonlinear atmospheric gravity wave behind a mountain (lee wave). In the shadowed region, the airflow associated with the wave is opposite to the ambient wind direction (adapted from [49]). The wind direction is defined here as the direction into which the wind is blowing.

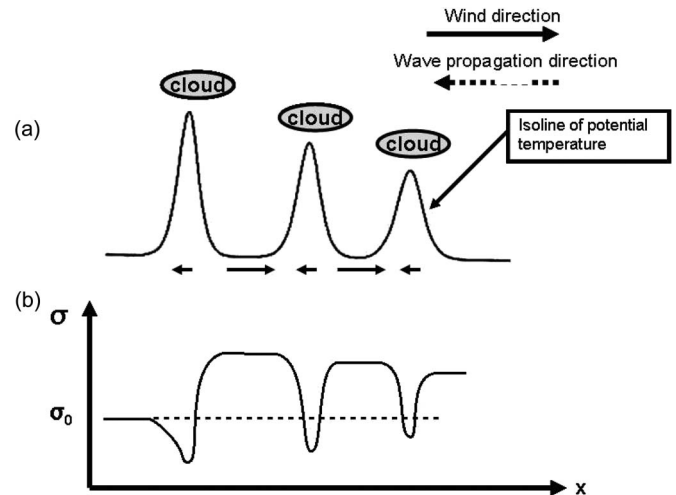


Fig. 3. Schematic diagram illustrating the generation of the radar signature of a strongly nonlinear atmospheric wave packet consisting of three solitons of elevation. (a) Shape of an isoline of potential temperature. The arrows below the isoline denote the direction and the magnitude of the surface wind associated with the waves. The wind direction is defined here as the direction into which the wind is blowing. (b) Variation of the normalized radar cross section  $\sigma$  (or equivalently of the radar image intensity) caused by the solitary waves.  $\sigma_0$  denotes the background NRCS. Clouds are located over the low NRCS areas.

this direction. Note also that the velocity of the airflow at the sea surface between two solitons of elevation is much larger than under the solitons of elevation.

The lower plot (b) in Fig. 3 shows the variation of the NRCS (or equivalently: of the radar image intensity) caused by the wave packet consisting of three solitary waves for the case that the ambient airflow has a component opposite to the wave propagation direction. In this plot,  $\sigma_0$  denotes the background NRCS caused by the background wind. Since the NRCS for wind speeds below  $25 \text{ m} \cdot \text{s}^{-1}$  is a monotonic function of wind speed [42], an increase (decrease) in sea surface wind speed leads in this wind speed range to an increase (decrease) in NRCS and, thus, to an increase (decrease) in image intensity or image brightness. Thus, this nonlinear AGW packet shows up



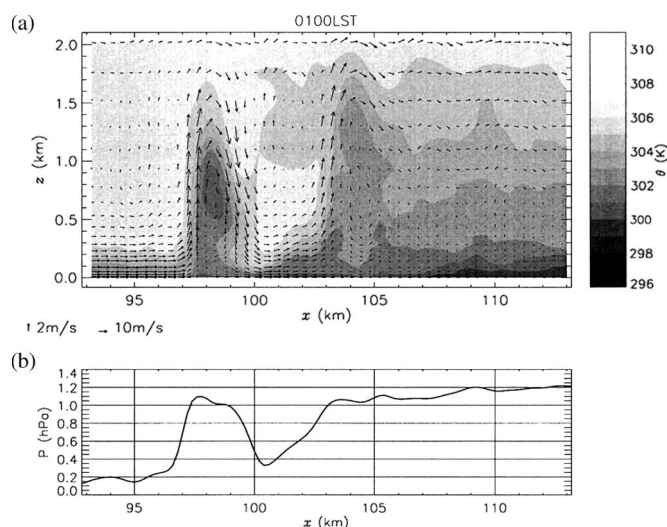


Fig. 4. Computer simulation carried out by Goler and Reeder [50] showing (a) the potential temperature and velocity vector fields and (b) the surface pressure associated with a Morning Glory solitary wave as it propagates from land onto the Gulf of Carpentaria. Note the low surface winds under the two solitons of elevation, giving rise to narrow dark bands on SAR image and the strong surface winds between them giving rise to a broad bright band.

in the SAR image as a weak narrow dark band in front followed by a broad bright band, which is then followed again by a weak narrow dark band. This feature is repeated, but with reduced image intensity modulation, for the subsequent solitary waves toward the rear of the wave packet. If the moisture content of the air is such that it allows the formation of clouds, then we expect that the clouds are positioned over the wave crests.

Note that the shape of NRCS pattern depicted in Fig. 3(b) requires that the airflow of the ambient wind has a velocity component, which is antiparallel to the wave propagation direction. If this direction were reversed, then the shape of the NRCS pattern would have also been reversed. However, this almost never seems to happen. So far, we have never found on ERS SAR or Envisat ASAR image a pattern (a narrow weak bright band in front followed by a broad dark band, which is followed again by a weak narrow bright band), which we could associate with nonlinear AGWs. Over the open ocean, AGWs are usually excited by cold fronts (often associated with thunderstorms) advancing against a warmer air mass. The cooler air undercuts the warm air and, thus, causes a disturbance that generates waves that propagate on the stable layer behind the cold front.

The airflow associated with solitary AGWs has been studied by computer simulations by many modelers. In Fig. 4, an example of such a simulation, which was carried out by Goler and Reeder [50] for a Morning Glory event, is depicted. These authors have shown that the Morning Glory is generated by the interaction of two sea breezes. AGWs develop as the cooler west-coast sea breeze undercuts the warmer (and deeper) east-coast sea breeze. In their calculations, they assume an ambient easterly airflow of  $5 \text{ m} \cdot \text{s}^{-1}$ . This is consistent with the observation that the Morning Glories propagating toward southwest are commonly observed when the geostrophic flow has an easterly component over Cape York Peninsula, Australia. Furthermore, it is also consistent with our assumption about the direction of the ambient airflow [see plot of Fig. 3(b)].

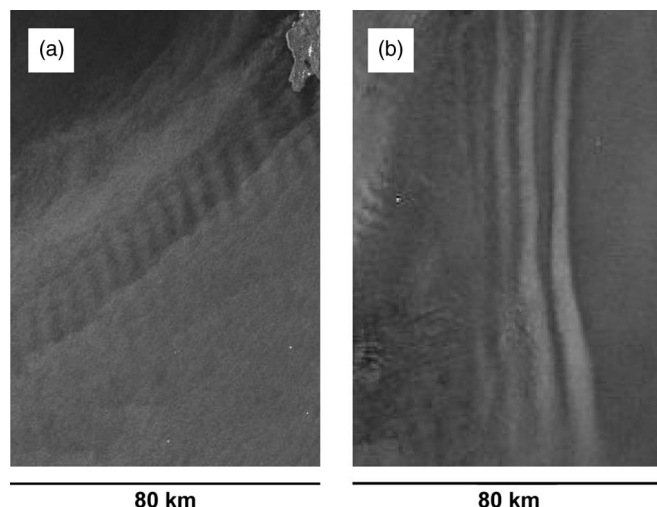


Fig. 5. Envisat ASAR images showing radar signatures of AGWs. (a) Envisat ASAR image acquired in the alternating polarization mode over the Strait of Taiwan on November 21, 2005, at 1402 UTC. Visible is in the upper right-hand corner the southern tip of Taiwan and in the diagonal are visible radar signatures of an AGW wave train, which was generated by the interaction of a northeasterly wind with the mountain range of southern Taiwan. (b) Envisat ASAR WS image acquired in the WS mode over the Indian Ocean off the east coast of South Africa on January 16, 2007, at 2027 UTC. Visible are radar signatures of an AGW packet consisting of three solitons, which was generated by an atmospheric front.

The AGWs generated by the interaction of two sea breezes over Cape York Peninsula propagate westward into the marine boundary layer over the Gulf of Carpentaria. The upper plot of Fig. 4 shows the potential temperature and velocity vector fields and the lower plot the surface pressure associated with this AGW as it propagates from land onto the Gulf of Carpentaria. The shading represents the potential temperature field and the arrows represent the velocity vectors. Note the strong recirculation zone under the leading soliton and the pressure jump associated with it. Under the two solitons of elevation, the sea surface wind speed is very low and, when superimposed on the ambient airflow, should give rise to two narrow bands of reduced image brightness. Between two solitons of elevation, the wind speed is increased such that this region should appear as a broad bright band on the SAR image. Indeed, such an image brightness modulation pattern is observed on a SAR image showing sea surface signatures of the Morning Glory (Fig. 14).

In Fig. 5, two Envisat ASAR images showing typical radar signatures of nonlinear AGWs are depicted, confirming the theoretical considerations presented in this section. The left SAR image (a) shows radar signatures of a weakly nonlinear lee wave that was generated by the interaction of airflow with a mountain range [18], and the right SAR image (b) shows radar signatures of a strongly nonlinear AGW packet, consisting of three solitons, that was generated by an atmospheric front.

Furthermore, there is ample observational evidence that the cloud bands (when present) are located above the wave crests, as depicted in Fig. 3. We have confirmed this by comparing simultaneously acquired Envisat ASAR and Envisat Medium Resolution Imaging Spectrometer (MERIS) images showing solitary AGW signatures in the sea surface roughness pattern and in the cloud pattern. Indeed, the clouds are

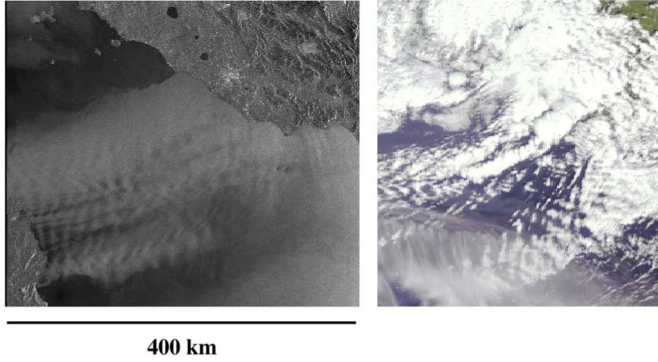


Fig. 6. Envisat ASAR WS image (left) and Envisat MERIS image (right) acquired at the same time on February 24, 2004, at 0920 UTC over the Tyrrhenian Sea (Mediterranean Sea) between Sardinia and the Italian Peninsula showing wave patterns on the ASAR image as well as on the MERIS image. The wave patterns visible on the ASAR image are caused by sea surface roughness modulation and the ones on the MERIS image by the cloud distribution induced by AGWs.

located above the dark bands visible on the ASAR images. Fig. 6 shows such an example. These images were acquired exactly at the same time on February 24, 2004, at 0920 UTC (Universal Time Coordinated) over the Tyrrhenian Sea (Mediterranean Sea) between the Italian island Sardinia and the Italian Peninsula, showing wave patterns on the SAR image as well as on the MERIS image. By overlaying the ASAR image with the MERIS image using the BEAM software (<http://www.brockmann-consult.de/cms/web/beam>), we could show that the wavelengths of the wave patterns on both images are approximately equal and that the clouds are located over the dark bands. This implies that the clouds are located at positions where the isolines of potential temperature have their maxima [see Fig. 3(a)].

### III. RADAR SIGNATURES OF OIW's

As mentioned before, OIW's become visible in SAR images (provided that they were not acquired over nonsurface slick infested sea areas) by the variation of the sea surface roughness caused by variations of the surface current associated with these waves. Theoretical models describing the modulation of the short-scale sea surface roughness by the variable surface currents have been developed previously in the framework of weak hydrodynamic interaction theory [19], [20], [51]. When using the weak hydrodynamic interaction theory, as described in [20], together with Bragg scattering theory, which relates spectral values of the ocean surface waves to NRCS values [52], the relationship between NRCS and surface current gradient  $U_x/dx$  can be written as [20]

$$\sigma = \sigma_0(1 + A dU_x/dx) \quad (2)$$

where  $\sigma$  denotes the total NRCS,  $\sigma_0$  is the NRCS of the background,  $x$  is the coordinate in the direction of the look direction of the SAR antenna projected onto the horizontal plane, and  $A$  is a constant that depends on radar wavelength, incidence angle, and the relaxation rate. The relaxation rate is quite variable. It depends, among others, on wind speed and wind direction. The gradient  $dU_x/dx$  is related to OIW and upper ocean parameters,

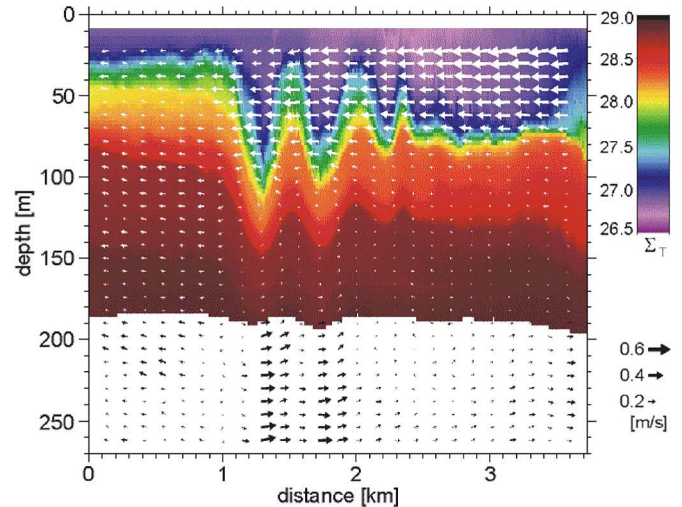


Fig. 7. Density and current distributions measured in the Mediterranean Sea north of the Strait of Messina ( $38.3^\circ$  N,  $15.7^\circ$  E) during the passage of a northward propagating packet of solitary oceanic internal waves. The density distribution was measured by a CTD chain and the current distribution by an acoustic Doppler current profiler from the research ship "Alliance." Note the three pronounced solitary waves of depression.

like amplitude and wavelength of the OIW and the stratification of the water layer. The larger the amplitude of the OIW is, the larger  $dU_x/dx$  becomes. In (2), we see that the NRCS is increased in convergent flow regions and is decreased in divergent flow regions. Consequently, the radar signature of a linear OIW manifests itself on the radar image as bands of increased and decreased image intensity relative to a background (see [20, Fig. 2] or <http://www.ifm.zmaw.de/fileadmin/files/ers-sar/Sdata/oceanic/intwaves/index.html>).

For linear OIW's, the image brightness pattern has a sinusoidal shape consisting of successive bands of increased and decreased image brightness with equal widths.

A more advanced radar imaging theory of OIW's based also on weak hydrodynamic interaction theory, but taking into account the hydrodynamic modulation of intermediate-scale surface waves and the interaction of these waves with the short surface waves [51], yields qualitatively similar results [21]. In this theory, the variation of the NRCS or image intensity, also called modulation depth, depends strongly on wind speed and direction. The higher the wind speed is, the smaller the modulation depth becomes. When the wind speed is above  $10 \text{ m} \cdot \text{s}^{-1}$ , the modulation depth is so small that practically no OIW patterns can be delineated anymore on SAR images of the sea surface.

Most of the OIW's that leave fingerprints on the sea surface are highly nonlinear. As their AGW counterparts, they usually occur in wave packets consisting of several solitons (see Fig. 7). According to the soliton theory, the solitary OIW's are solitons of depression when the water depth is larger than twice the depth of the pycnocline (interface between the water layers of different densities in a two-layer water body). This condition is fulfilled in most regions of the world's oceans, where solitary OIW's are encountered. However, a prominent exception is the shelf region of the South China Sea between Dongsha Island and the Chinese coast, where occasionally solitary OIW's of elevation have been detected [32]. However, a transformation

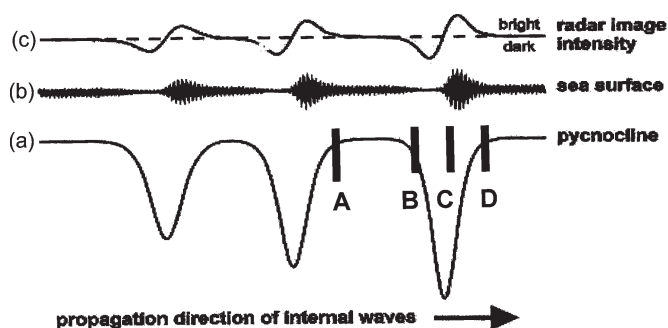


Fig. 8. Schematic diagram illustrating the generation of the radar signature of a nonlinear oceanic internal wave packet consisting of three solitons of depression. (a) Shape of the pycnocline in a two-layer model. (b) Variation of the short scale sea surface roughness. (c) Variation of the radar image intensity (image brightness). The distances B–C and C–D give the widths of the bands with decreased and increased image brightness, respectively, and A–B the width of the band with background image brightness.

of solitary waves of depression into solitary waves of elevation occurs quite seldom in the ocean. When solitary waves travel into a shelf region, they usually break and generate secondary solitary waves or turbulence [53]. Only when the shelf is broad and has a very gentle slope may such a transformation from solitary waves of depression to solitary waves of elevation take place. As far as we know, such a transformation has only been reported from the shelf of the South China Sea and from no other region in the world's oceans so far.

Fig. 7 shows a typical water density profile associated with a strongly nonlinear OIW packet consisting of three solitons of depression. (More precisely, the profile shows an undular bore because the density profile before the passage of the nonlinear disturbance has not relaxed to the same level. This profile was measured in the Mediterranean Sea north of the Strait of Messina (38.3° N, 15.7° E) from a ship using a conductivity, temperature, and depth (CTD) chain (courtesy of J. Sellschopp, FWG, Kiel). Inserted in this plot is also the current distribution that was measured by an acoustic Doppler current profiler.

In analogy to the schematic diagram depicted in Fig. 3, which applies to AGW, Fig. 8 shows a similar schematic diagram for OIW<sub>s</sub> illustrating the generation of the radar signature of a nonlinear OIW wave packet consisting of three solitons of depression. Line (a) in Fig. 8 shows the shape of the pycnocline for the case that the ocean has only two layers of different water density. The inserted vertical lines mark the boundaries of the regions where the surface current is convergent (between C and D), where it is divergent (between B and C), and where it does not vary (between A and B). Note that the widths of the convergent and divergent flow regions (C–D and B–C) are much smaller than the width of the region with no current variations. Line (b) in Fig. 8 shows the variation of the short scale sea surface roughness (amplitude of the Bragg waves), which determines the variation of the backscattered radar power or the NRCS. Finally, line (c) in Fig. 8 shows the variation of the radar image intensity (or the NRCS) caused by the solitary OIW<sub>s</sub> of depression.

The wave packet consisting of solitary OIW<sub>s</sub> of depression shows up in a SAR image as a narrow bright band in front followed by a narrow dark band. Then, a much wider band

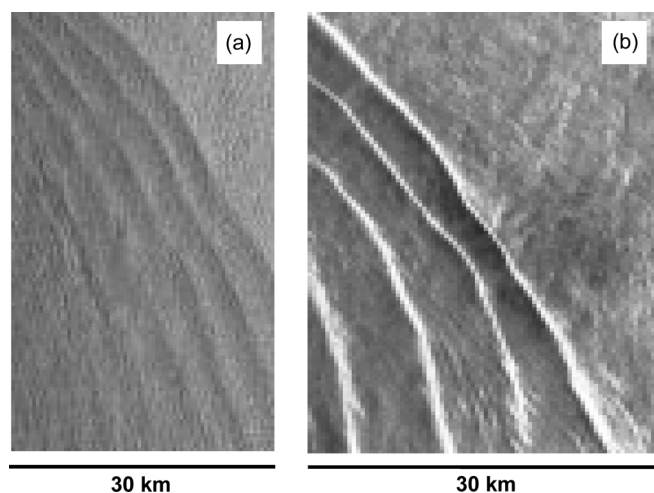


Fig. 9. Two typical SAR images acquired over the Andaman Sea in the Indian Ocean showing radar signatures of nonlinear OIW packets. (a) An Envisat ASAR image acquired in the image mode (IM) on May 10, 2006, at 0329 UTC. (b) An ERS-2 SAR image acquired on February 11, 1997, at 0359 UTC.

of average (background) image brightness with no modulation follows. This structure is repeated for the other solitary waves toward the rear of the wave packet, but with reduced image intensity modulation due to the smaller amplitudes of the successive solitons in the packet. Furthermore, the distances between the solitons decrease from front to rear in the packet. If the wave packet consists of solitary OIW<sub>s</sub> of elevation, then the modulation pattern starts with a narrow dark band in front followed by a narrow bright band. Such a modulation pattern has been observed in SAR images acquired over the continental shelf region in the South China Sea [32].

In Fig. 9, two typical SAR images acquired over the Andaman Sea in the Indian Ocean showing radar signatures of nonlinear OIW packets are depicted. The image on the left shows the typical modulation pattern as predicted by theory (Fig. 8). Here, the modulation depth [difference between maximum and minimum deviation from the average (background) value] caused by the solitary OIW<sub>s</sub> is relatively moderate. However, the image on the right (reproduced from [39]) shows a very bright line in front indicating that here the modulation of the radar backscatter is very strong, very likely due to strong breaking of surface waves induced by the solitary OIW<sub>s</sub>. It is a general observation that we have made when analyzing SAR images: When strong solitary OIW<sub>s</sub> are imaged, the dark line following the strong bright line is usually very weak and sometimes even absent.

A radar imaging theory applicable for strong solitary OIW<sub>s</sub>, which includes wave breaking of surface waves, has been developed by Kudryavtsev *et al.* [22]. It takes into account scattering from the “regular” surface (by means of resonant Bragg scattering and specular reflections) and specular reflection from breaking waves. In this theory, wave breaking plays a central role. It contributes to the NRCS modulation not only by means of specular reflections from breaking surface waves, but also by means of Bragg scattering from additional short waves that are generated by them. However, in their model, the modulation depends strongly on wind speed and wind direction, and it will be difficult to extract OIW parameters from the strength of the



modulation unless the wind field and wind direction is precisely known at the site where the OIW's are observed. An expression for the change in NRCS  $\Delta\sigma_0$ , caused by a solitary OIW with width  $L$ , maximum surface current velocity  $U_{\max}$ , and phase speed  $C_i$ , has been derived from the theory of Kudryavtsev *et al.* [22] (Dagestad, private communication, 2009). It reads

$$\Delta\sigma_0 = \alpha \frac{U_{\max}}{W^2 L C_i}. \quad (3)$$

Here,  $W$  denotes the wind speed, and  $\alpha$  is a parameter dependent on wind direction. This expression shows, among others, that the modulation depth decreases with wind speed and increases with  $U_{\max}$  and, thus, with wave amplitude. However, it should be stressed that this theory is based on the modulation of wind waves by solitary OIW's. It requires the presence of wind speeds above the threshold for Bragg wave generation ( $2\text{--}3 \text{ m} \cdot \text{s}^{-1}$ ).

This condition, however, is not always fulfilled when strong surface signatures of solitary OIW's are observed on SAR images, particularly not in tropical and subtropical oceans, where the wind speed is often very low. Mariners have often observed sea surface signatures of strong solitary OIW's even when the sea surface was completely calm. Such observations of roughness bands on the sea surface, which they called rippings at that time, were described already in a book published in 1861 [54]. In this book, sea surface signatures of solitary OIW's in the Andaman Sea are described as follows: "The rippings are seen in calm weather approaching from a distance, and in the night their noise is heard a considerable time before they come near. They beat against the sides of the ship with great violence, and pass on, the spray sometimes coming on deck; and a small boat could not always resist the turbulence of these remarkable rippings."

In the light of these *in situ* observations, we are quite skeptical that even the most advanced theories on radar imaging of OIW's are able to extract quantitative information on the amplitude of strong solitary OIW's from the depth of the image intensity modulation. However, such information may be obtained from the characteristic width of radar signatures of solitary OIW's [55].

#### IV. REPRESENTATIVE EXAMPLES OF SAR IMAGES SHOWING RADAR SIGNATURES OF AGWs

The radar signatures of AGWs vary more than the ones of OIW's. To illustrate this, we present in this section 12 examples of SAR images showing radar signatures of AGWs (Figs. 10–17). These images were acquired by the SARs onboard the ERS-1, ERS-2, and the Envisat satellites between 1992 and 2009 over different regions of the world's oceans. For the Envisat ASAR image depicted in Fig. 10(a), we have a cloud image for comparison. This image was acquired in the visible band by the Japanese geostationary meteorological satellite Multifunctional Transport Satellite (MTSAT)-1R only 8 min later than the ASAR image [18] (not reproduced here). For the ERS-1 SAR image depicted in Fig. 12(a), we have quasi-simultaneously acquired *in situ* meteorological data, and for the Envisat ASAR images depicted in Fig. 15, we have a

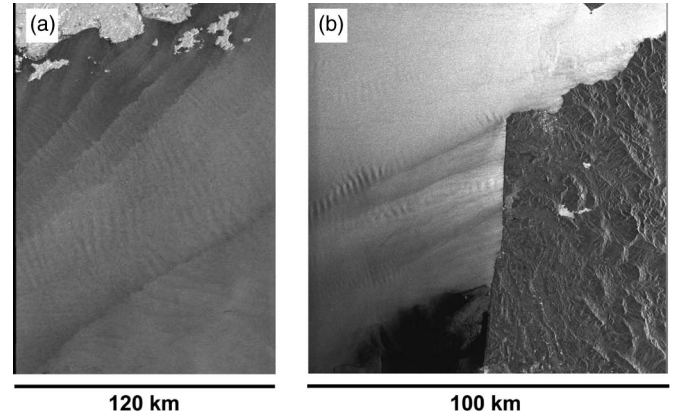


Fig. 10. (a) Envisat ASAR WS image acquired over the sea area southwest of Hong Kong on March 8, 2007, at 0222 UTC. Visible are sea surface signatures of wind shear lines and of atmospheric gravity waves. (b) ERS-2 SAR image acquired over the sea area west of the Strait of Gibraltar on June 6, 2000, at 1105 UTC. Visible are sea surface signatures of atmospheric gravity waves generated by an easterly wind blowing through the Strait of Gibraltar and over northern Morocco. The wave train to the north is generated by a horizontal shear in the wind field and the other wave trains are typically lee waves generated by the interaction of the wind with topographic features at the Moroccan Atlantic coast.

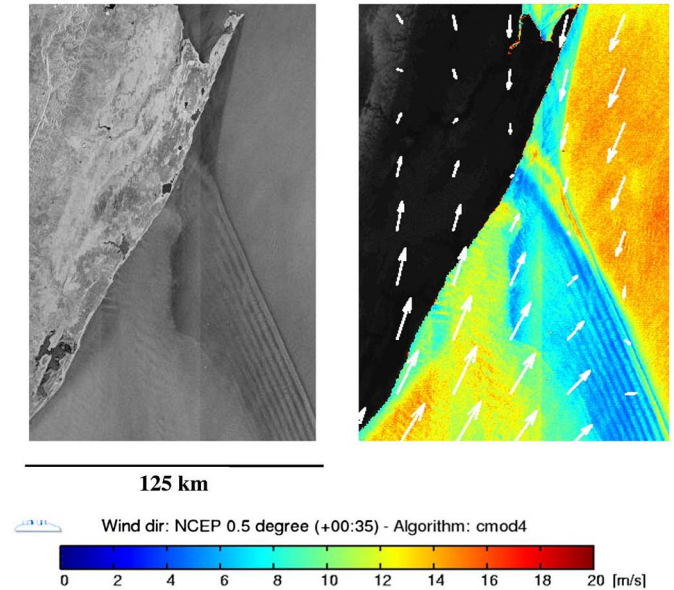


Fig. 11. (a) Envisat ASAR WS image acquired over the sea area off the east coast of South Africa on October 7, 2009, at 2024 UTC showing an AGW packet propagating northeastwards. (b) Near-surface wind field derived from the ASAR image by using the wind direction provided by the NCEP model (courtesy of the Nansen Environmental and Remote Sensing Center, Bergen). It shows that the AGWs were generated at an atmospheric (wind) front and that the waves are propagating against the ambient wind. Note that the wave pattern has the classical structure shown in Fig. 3.

cloud image, which was acquired in the infrared band by the MODIS sensor onboard the Terra satellite only 4 min later than by the ASAR.

The SAR image depicted in Fig. 11(a) was acquired by the Envisat ASAR in the wide swath (WS) mode over the sea area off the east coast of South Africa on October 7, 2009, at 2024 UTC. Visible is an AGW packet consisting of seven solitons propagating northeastward. The near-surface wind field derived from the ASAR image by using the wind direction

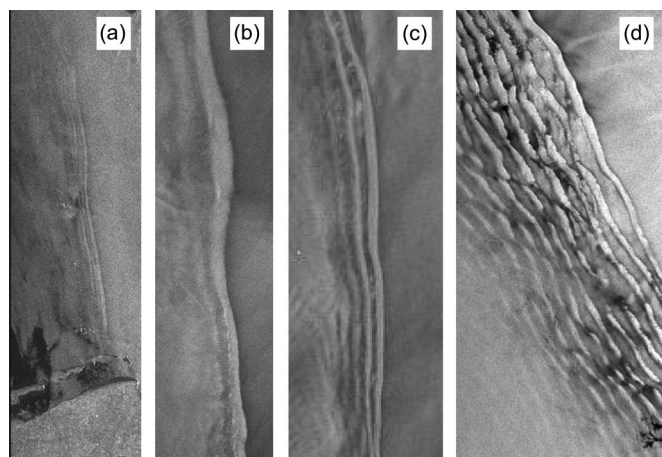


Fig. 12. SAR images acquired over different sea areas showing sea surface signatures of solitary AGWs that have the structure as predicted by the SAR imaging theory (Fig. 3). In all cases, the width of the imaged areas is 40 km. (a) ERS-1 SAR image acquired over the North Sea on March 8, 1992, at 1025 UTC. (b) Envisat ASAR IM image acquired over the North Atlantic off the coast of Morocco on February 9, 2006, at 2214 UTC. (c) Envisat ASAR WS image acquired over the Black Sea on February 13, 2009, at 1923 UTC. (d) ERS-1 SAR image acquired over the Caspian Sea on May 12, 1996, at 0723 UTC.

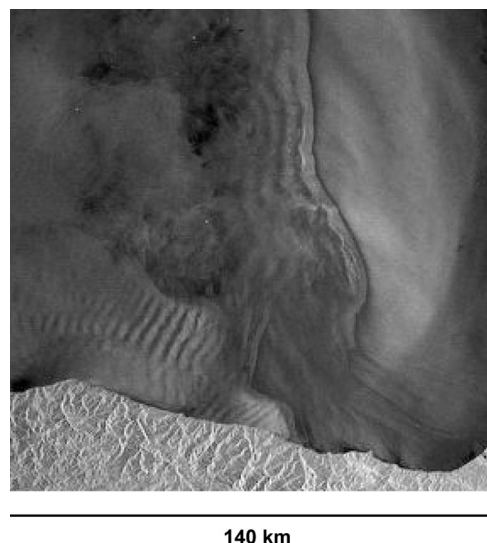


Fig. 13. Envisat ASAR WS image acquired over the Black Sea off the northern coast of Turkey on May 31, 2007, at 1935 UTC showing simultaneously sea surface signatures of solitary AGWs and quasi-linear AGWs. Note that the bright bands are always broader than the dark lines.

provided by the NCEP model (35 min later) is depicted in Fig. 11(b). The wind speed at the front of the AGW packet varies between 6 and  $13 \text{ m} \cdot \text{s}^{-1}$ . Thus, wind fluctuation induced by the AGWs is about  $7 \text{ m} \cdot \text{s}^{-1}$ . Since the wave pattern is located near a wind front, it is safe to assume that the pattern results from AGWs generated by strong wind shear associated with this front. The waves propagate against an ambient wind having a speed of around  $13 \text{ m} \cdot \text{s}^{-1}$ . Note that the wave pattern complies quite well with the  $\sigma$ -profile shown in Fig. 3(b) (broad bright bands bordered by narrow bands and a dark band at the front of the packet).

The ERS-1 SAR image depicted in Fig. 12(a) was acquired over the German Bight of the North Sea on March 8, 1992, at



Fig. 14. Envisat ASAR WS image acquired over the Gulf of Carpentaria (northern Australia) on September 19, 2004, at 1303 UTC showing sea surface signatures of a Morning Glory solitary wave. Note the broad bright band bordered by two narrow dark bands as predicted by theory (Fig. 3) and by simulations (Fig. 4).

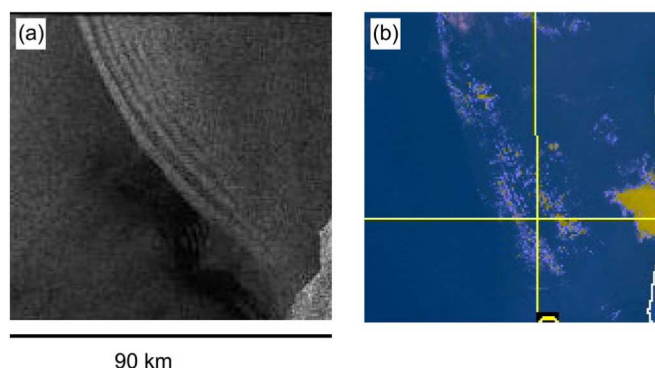


Fig. 15. (a) Envisat ASAR image acquired in the global mode over the Gulf of Carpentaria (northern Australia) on November 17, 2006, at 1259 UTC showing sea surface signatures of a "Morning Glory" atmospheric gravity wave packet. Note the broad bright bands bordered by two narrow dark bands as predicted by theory (Fig. 3). (b) MODIS thermal composite image acquired over the same area on November 17, 2006, at 1303 UTC showing wave patterns associated with the atmospheric gravity wave packet in the cloud temperature.

1025 UTC. For this event, nearly simultaneous meteorological data (wind speed and direction, temperature, and pressure) were available from an 80-m-high mast located on the island of Helgoland [11]. These data clearly show that an AGW packet passed the tower 27 min before the SAR data acquisition. Also in this case, the waves propagated against an ambient wind direction giving rise to the  $\sigma$ -profile shown in Fig. 3(b).

For all other SAR images presented in this section, we do not have quasi-simultaneously data for supporting our hypothesis that the wave patterns visible on the SAR images are, indeed, radar signatures of AGWs. However, based on previous analyses of SAR data, we are confident that all of them show radar signatures of AGWs. We have compared these SAR images



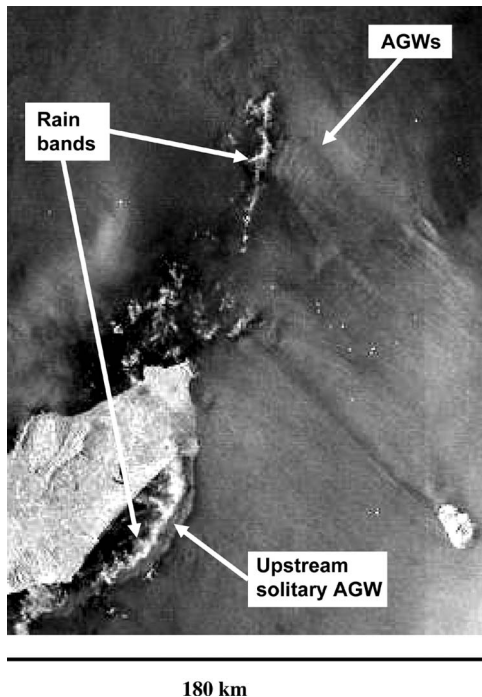


Fig. 16. Envisat ASAR image acquired in the WS mode over the Mediterranean Sea north of Tunisia on May 12, 2008, at 2108 UTC showing radar signatures of rain bands and AGWs. The wind was blowing from southeast with a speed of  $12 \text{ m} \cdot \text{s}^{-1}$ .

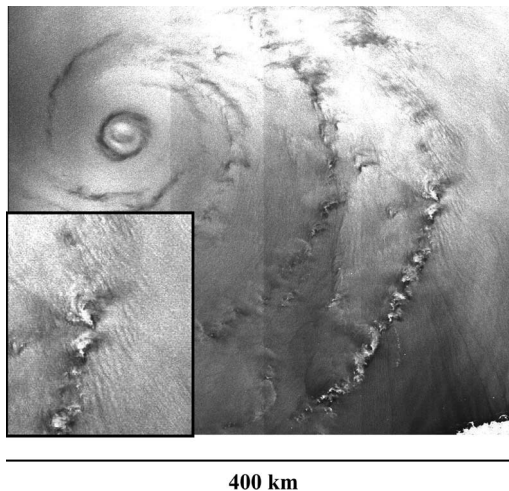


Fig. 17. Envisat ASAR WS image acquired over the Gulf of Mexico on September 22, 2005, at 0344 UTC showing radar signatures of the hurricane Rita. Visible are radar signatures of the eye of the hurricane, of rain cells organized in rain bands, and of AGWs. Inserted is a zoom of the area east southeast of the hurricane eye showing pronounced radar signatures of AGWs.

with wind fields retrieved from QuikScat data, with NCEP wind fields, and with weather charts and found that the wave patterns visible on the SAR images depicted in Figs. 11–13 were all located at or near strong atmospheric fronts. This suggests that the wave patterns are radar signatures of solitary AGWs were generated by atmospheric fronts. The AGW visible on the ERS-2 SAR image depicted in Fig. 10(b) was generated by wind shear associated with the easterly wind blowing through the Strait of Gibraltar and interacting with the Moroccan coast. The sea surface pattern visible on the ASAR image depicted in Fig. 14 is

located in an area (the Gulf of Carpentaria), where mostly south westward propagating solitary AGWs, here called Morning Glories, are observed in cloud patterns. Furthermore, the shape of the pattern compares favorably well with the simulations depicted in Fig. 4. The only other ASAR image of a Morning Glory, which we have found in the ERS/Envisat SAR archive, is depicted in Fig. 15(a). In this case, the Morning Glory consists of several solitons. For this event, we have for comparison a near simultaneous thermal composite (night) image that shows the presence of the AGW packet in the cloud pattern by means of temperature variations.

AGWs are generated not only by winds interacting with mountain ranges, but also by collision of different air masses at atmospheric fronts, strong wind shear at coast lines, and convective activities associated with thunderstorms [56]–[59]. Of course, we cannot detect thunderstorms by SAR, but we can detect rain cells and rain bands [60]–[64], which are often associated with thunderstorms. Fig. 16 shows an Envisat ASAR WS image acquired over the Mediterranean Sea between Tunisia and Sicily on May 12, 2008, at 2108 UTC. Visible in the upper section of the SAR image are radar signatures of a rain band and of AGWs located adjacent to the rain band on the southwest (upwind) side. Furthermore, visible in the lower left section of the SAR image is the Tunisian Peninsula Maouin. The bright band off its east coast is very likely the radar signature of a strong rain band caused by volume scattering at rain drops in the atmosphere. This interpretation is supported by the observation that this radar signature extends to the north also over land. We interpret the feature on the east/southeast side of the rain band as the radar signature of an upstream solitary AGW since it has a dark band in front followed by a bright band. A close inspection of the SAR image reveals that between the radar signatures of the rain band and the aforementioned solitary wave, the radar signature of a second solitary wave is visible in the central section. The wind was blowing from southeast as inferred from the wake behind the Italian island of Pantelleria (in the lower right hand section of the image SAR image) and also as predicted by the NCEP model. In the wind wake of this island, weak radar signatures of AGWs can also be delineated, which further supports our supposition that the other wave patterns visible on this ASAR image are, indeed, radar signatures of AGWs. By applying the CMOD4 model, we infer that the SAR-retrieved wind speed is  $12 \text{ m} \cdot \text{s}^{-1}$ .

Radar signatures of AGWs are visible on SAR images even when the wind speed is extremely high, as in hurricanes. In Fig. 17, an Envisat ASAR WS image is depicted, which was acquired over the Gulf of Mexico on September 22, 2005, at 0344 UTC. This image shows radar signatures of the hurricane Rita. Visible are radar signatures of the eye of the hurricane, of rain cells organized in rain bands, and of AGWs. The insert shows a zoom of the area east southeast of the hurricane eye on which pronounced radar signatures of AGWs are visible. The wavelengths of the AGWs are around 4.5 km. It is well known that strong updrafts encountered in hurricanes and typhoons can generate AGWs. For example, a cloud image acquired by the MODIS (Moderate Resolution Imaging Spectroradiometer) onboard the Terra satellite over the Gulf of Mexico during

the passage of the hurricane Katrina on August 27, 2005, has revealed the presence of AGWs in the cloud pattern (<http://earthobservatory.nasa.gov/IOTD/view.php?id=5808>).

## V. DISCRIMINATION BETWEEN RADAR SIGNATURES OF AGWs AND OIW<sub>s</sub>

Wave-like patterns visible on SAR images of the sea surface can be radar signatures of AGWs, OIW<sub>s</sub>, sandbanks, or atmospheric boundary layer rolls. Radar signatures originating from sandbanks or of atmospheric boundary layer rolls can, in general, be identified quite easily and will not be treated in this paper in detail (see, e.g., [65]–[67]). When the sea surface signatures result from sandbanks, they can only be encountered in shallow water areas where periodically spaced sandbanks and strong cross-sandbank currents (usually of tidal origin) are known to exist [65]. When they result from boundary layer rolls, the wave pattern is aligned approximately in wind direction, and the spacing in cross-wind direction between the individual rolls increases in the downwind direction [67].

To identify unambiguously wave patterns visible on SAR images as radar signatures of AGWs or OIW<sub>s</sub>, one needs, in general, auxiliary information, e.g., on the geographical location of the wave pattern, on the state of the ocean and the atmosphere, on coastal topography, and on underwater bottom topography. Often, however, one can already decide, with a high probability, from the shape and structure of the wave pattern whether it originates from AGWs or OIW<sub>s</sub>. The more nonlinear the waves are, the easier this becomes. Quasi-linear OIW<sub>s</sub> are seldom observed on SAR images because the gradient in sea surface velocity associated with these waves is too small to cause sufficiently large NRCS modulations.

However, nonlinear OIW packets usually give rise to large NRCS modulations when the wind speed is low. In a SAR image, a nonlinear OIW packet manifests itself as a convex wave pattern with a narrow bright band in front followed by a narrow dark band. Often, the narrow dark band is only faintly visible. The larger the amplitude of the solitary OIW, the brighter is the narrow bright band (usually a consequence of wave breaking of the surface waves) and the narrower its width become. This double-sign structure of the radar signature of the leading solitary OIW in a wave packet (narrow right band followed by narrow band) is then repeated with smaller modulation depths for the subsequent solitary waves in the wave packet. The radar signatures of the solitary OIW<sub>s</sub> in the wave packet are usually separated by a broad band of average background image brightness.

On the other hand, the wave pattern resulting from nonlinear AGW packets starts with a narrow (often weak) dark band in front followed by a broad bright band, which is then followed again by a narrow dark band. This structure (broad bright band sandwiched in between two narrow dark bands) is then repeated with less modulation depths for the subsequent solitary waves in the AGW packet. Note that the width of solitary OIW<sub>s</sub> as well as of solitary AGWs is related to its amplitude. In general, the smaller the width is, the larger the amplitude becomes. However, this is only true over a limited parameter range [68].

Contrary to OIW<sub>s</sub> visible on SAR images, which are in most cases highly nonlinear and appear in wave packets with a sharp front, the AGWs visible on SAR images imaged by SAR are often quasi-linear. This makes it easier to identify OIW on SAR images than AGWs. In general, the radar signatures of OIW<sub>s</sub> are more “crisp” than the ones of AGWs, which are smoother.

Another observation that often helps in the discrimination of radar signatures of AGWs and OIW<sub>s</sub> is the difference in wind speed dependence. While radar signatures of AGWs are observed at all wind speeds, even at hurricane-force wind speeds, strong radar signatures of OIW<sub>s</sub> are observed only at low wind speeds, and weak radar signatures are observed at moderate wind speeds of less than  $10 \text{ m} \cdot \text{s}^{-1}$ . Above wind speeds of  $10 \text{ m} \cdot \text{s}^{-1}$ , the radar signatures of OIW<sub>s</sub> are so weak that practically no OIW<sub>s</sub> can be detected on SAR images [69].

### A. Criteria Based on the Structure and Shape of the Radar Signatures

The following criteria can be applied for discriminating between radar signatures of solitary OIW<sub>s</sub> and solitary AGWs.

- 1) If the wave-like pattern visible on the radar image starts with a bright band in front followed by a narrow dark line (unless encountered in special areas where OIW<sub>s</sub> of elevation can exist) and if the area between the double-sign structure of the radar signature of a solitary OIW has average background brightness, then the wave-like pattern results from a nonlinear OIW packet [see Fig. 9(b)].
- 2) If the pattern at the front of a wave packet consists of a bright band bordered by two narrow dark bands, then this is very likely the radar signature of the leading solitary wave in an AGW packet (see Figs. 5(b), 6, 11(a), 12(a)–(d), 13, 14, and 15).
- 3) If the wave pattern is quasi-sinusoidal or if the bright bands are broader than the dark bands, then the pattern results from a weakly nonlinear AGW (see Figs. 5(a), 10(a), 13, and 16).
- 4) If the wave pattern has a large modulation depth and is located in an area where the wind speed is above  $10 \text{ m} \cdot \text{s}^{-1}$ , then it originates from an AGW.

Another criterion that could be applied is to exploit the polarization diversity of the radar signatures of AGWs and OIW<sub>s</sub>. If the modulation depth of the wave pattern is stronger on SAR images acquired at HH polarization than at VV polarization, then the pattern originates from OIW<sub>s</sub>. According to conventional SAR imaging theory of OIW<sub>s</sub> based on weak hydrodynamic interaction theory [51], the modulation depth is larger for HH polarization than for VV polarization (see also [70] and [71]). The same result is obtained from Kudryavtsev’s radar imaging theory of current features [22]. On the other hand, if the wave pattern originates from AGWs, the modulation depth is, to first order, independent of polarization. However, in practice, this criterion is of limited use because multipolarization SAR data are presently available from satellites only when the SAR operates in a reduced swath-width mode, which compromises its utility for coverage. Furthermore, the difference in modulation depth at both polarizations is usually quite small for large-amplitude solitary OIW<sub>s</sub> because the radar backscattering is

dominated by scattering at breaking surface waves, which is independent of polarization [22].

### B. Criteria Based on Other Information

There also exist criteria other than the shape and structure of the radar signatures by which the origin of the wave pattern can be determined with a high degree of confidence.

*a) Criteria in Favor of AGWs:* The wave pattern originates very likely from AGWs if the pattern

- 1) is located in the lee of a mountainous island or a mountainous coast [see Figs. 5(a), 6, and 10(a)];
- 2) is intersected by land, e.g., by a peninsula, and the radar signatures are visible on the sea on both sides;
- 3) is located near an atmospheric front (usually a cold front) [see Figs. 5(b), 11(a), and 12(a)–(d)];
- 4) is located at a strong wind shear zone [see Fig. 10(a) and (b)];
- 5) is located in a sea area with no shallow underwater bottom topography, no strong currents (usually tidal), and no upwelling and where the water column is not stratified such that no OIW's are supported;
- 6) matches the wave pattern visible on a quasi-simultaneously acquired cloud image [see Figs. 6, 10(a), and 15(a)].

*b) Criteria in Favor of OIW's:* The wave pattern originates very likely from OIW's if the pattern

- 1) is located in a sea area where
  - a) the water column is strongly stratified;
  - b) shallow underwater ridges, sea mounts, or steep shelf breaks are present;
  - c) where strong (tidal) currents are known to exist;
- 2) is located near an upwelling region;
- 3) consists of regularly spaced wave packets with inter-packet separations ranging from 15 to 120 km.

Regularly spaced wave packets are observed when the internal oceanic waves are tidally generated (usually by the semidiurnal tide that has a period of 12.4 h).

To increase the probability further to interpret the wave pattern correctly, one should check whether the lower atmosphere was able to support AGWs. For this, one can use radiosonde data that are available online from the website of the University of Wyoming, Laramie, WY (<http://weather.uwyo.edu/upperair/sounding.html>). From these data, one can calculate the following (see, e.g., [7], [17], and [18]):

- 1) the vertical profile of the potential temperature from which one can determine whether the air column was stratified [70];
- 2) the Scorer parameter [17], [18], [71] and the Richardson number [18], which provide necessary conditions for vertical trapping of AGWs in the lower atmosphere.

However, often, radiosonde data are only available 1) from locations that are quite far from the location of the sea area imaged by SAR and 2) at times that seldom match sufficiently well the time of the SAR data acquisition. Furthermore, they provide only necessary conditions for the existence of AGWs trapped in the lower troposphere and are therefore only of

limited value for discriminating between radar signatures of AGWs and OIW's.

## VI. CONCLUSION

Radar signatures of AGWs and OIW's visible on SAR images of the sea surface often look quite similar, which has led to many misinterpretations in the past. We have applied known theories of radar imaging of mesoscale atmospheric and oceanic phenomena to radar imaging of AGWs and OIW's and have derived in Section V-A several criteria based on the shape and the structure of the radar signatures that can be used for discrimination. They should be sufficient in many cases. In Section V-B, we have listed several other criteria to supplement discrimination between the radar signatures of these two types of waves. They concern the geographical location of the wave-like pattern and the states of the atmosphere and ocean at the location and time of the SAR data acquisition. Sometimes, wave patterns visible on SAR images are matched by wave patterns visible on quasi-simultaneously acquired cloud images acquired in the visible or infrared bands. In these cases, the radar signature can be attributed unambiguously to AGWs.

By combining the criteria based on the structure and shape of the radar signature and other criteria listed in Section V-B, one should be able, in most cases, to discriminate between radar signatures of AGWs and OIW's. However, we have to concede that we have encountered several SAR images where we have been unable to decide whether the wave-like patterns originated from AGWs or OIW's. Reasons for such failures are manifold. They can result from the fact that the wave pattern is located in a sea area with an inhomogeneous roughness pattern caused, e.g., by a varying wind field and the presence of rain cells or surface slicks. Furthermore, the structure of the radar signatures of nonlinear OIW's can deviate from the structure depicted schematically in Fig. 8 because they do not result from mode 1 internal waves, but from mode 2 or higher mode internal waves. Another reason for a deviation can be a low-signal-to-noise ratio. The band of reduced sea surface roughness may not be visible on a SAR image because it has disappeared in the low image intensity background.

The number of parameters determining the radar signatures of AGWs and OIW's is quite large, and their values vary over a quite wide range. Therefore, it is impossible to attach firm numbers to the discrimination criteria presented in this paper. However, since the aim of this paper is only to provide remote sensing scientists with a tool on how to help distinguish between two options (AGWs or OIW's), such qualitative criteria should be appropriate. We do not claim that our discrimination criteria will always lead to unambiguous results, but we do hope that they will help oceanographers and meteorologists to greatly reduce the probability of misinterpreting wave patterns visible on SAR images of the sea surface.

## ACKNOWLEDGMENT

Part of this investigation was carried out when W. Alpers visited the State Key Laboratory of Satellite Ocean Environment Dynamics, Second Institute of Oceanography, State Oceanic

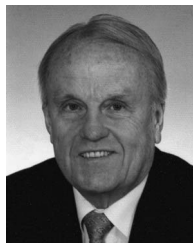


Administration, in Hangzhou, China. The financial support provided by this laboratory is greatly acknowledged. The authors would like to thank the European Space Agency for providing the ASAR images within the ESA-MOST Dragon 2 Program free of charge and K.-F. Dagestad of the Nansen Environmental and Remote Sensing Center, Bergen, Norway, for calculating the wind field from the ASAR image.

## REFERENCES

- [1] E. E. Gossard and W. H. Hook, *Waves in the Atmosphere*. New York: Elsevier, 1975.
- [2] R. K. Smith, "Travelling waves and bores in the lower atmosphere: The 'Morning Glory' and related phenomena," *Earth Sci. Rev.*, vol. 25, no. 4, pp. 267–290, Oct. 1988.
- [3] C. O. Hines, "Gravity waves in the atmosphere," *Nature*, vol. 239, no. 5367, pp. 73–78, Sep. 1972.
- [4] N. A. Crook, "Trapping of low-level gravity waves," *J. Atmos. Sci.*, vol. 45, no. 10, pp. 1533–1541, May 1988.
- [5] N. N. Romanova and I. G. Yakushkin, "Internal gravity waves in the lower atmosphere and sources of their generation (review)," *Atmos. Ocean. Phys.*, vol. 31, no. 2, pp. 151–172, Oct. 1995.
- [6] J. W. Rottman and R. Grimshaw, "Atmospheric internal gravity waves," in *Environmental Stratified Flows*, R. Grimshaw, Ed. Norwell, MA: Kluwer, 2002, pp. 61–88.
- [7] M. G. Wurtele, R. D. Sharman, and A. Datta, "Atmospheric lee waves," *Annu. Rev. Fluid Mech.*, vol. 28, pp. 429–476, 1996.
- [8] R. H. Clarke, R. K. Smith, and D. G. Reid, "The Morning Glory of the Gulf of Carpentaria: An atmospheric undular bore," *Mon. Weather Rev.*, vol. 109, no. 8, pp. 1726–1750, Aug. 1981.
- [9] D. R. Christie, "The Morning Glory of the Gulf of Carpentaria: Paradigm for non-linear waves in the lower atmosphere," *Aust. Meteorol. Mag.*, vol. 41, pp. 21–60, 1992.
- [10] P. W. Vachon, O. M. Johannessen, and J. A. Johannessen, "An ERS-1 synthetic aperture radar image of atmospheric lee waves," *J. Geophys. Res.*, vol. 99, no. C11, pp. 22 483–22 490, Nov. 1994.
- [11] W. Alpers and G. Stille, "Observation of a nonlinear wave disturbance in the marine atmosphere by the synthetic aperture radar on board the ERS-1 satellite," *J. Geophys. Res.*, vol. 101, no. C3, pp. 6513–6525, Mar. 1996.
- [12] Q. Zheng, X.-H. Yan, V. Klemas, C. R. Ho, N.-J. Kuo, and Z. Wang, "Coastal lee waves on ERS-1 SAR images," *J. Geophys. Res.*, vol. 103, no. C4, pp. 7979–7993, 1998.
- [13] R. M. Worthington, "Alignment of mountain lee waves viewed using NOAA AVHRR imagery, MST radar, and SAR," *Int. J. Remote Sens.*, vol. 22, no. 7, pp. 1361–1374, May 2001.
- [14] N. S. Winstead, T. D. Sikora, D. R. Thompson, and P. D. Mourad, "Direct influence of gravity waves on surface-layer stress during a cold air outbreak, as shown by synthetic aperture radar," *Mon. Weather Rev.*, vol. 130, no. 11, pp. 2764–2776, Nov. 2002.
- [15] X. Li, C. Dong, P. Clemente-Colon, W. G. Pichel, and K. Friedman, "Synthetic aperture radar observations of sea surface imprints of upstream atmospheric solitons generated by flow impeded by an island," *J. Geophys. Res.*, vol. 109, no. C2, p. C02 016, Feb. 2004. DOI:10.1029/2003JC002168.
- [16] W. Alpers, "Investigation of atmospheric gravity waves and rotors in the marine boundary layer using spaceborne synthetic aperture radar images," in *Proc. IEEE IGARSS*, Boston, MA, Jul. 6–11, 2008, vol. 4, pp. 57–60.
- [17] J. C. B. da Silva and J. M. Magalhaes, "Satellite observations of large atmospheric gravity waves in the Mozambique channel," *Int. J. Remote Sens.*, vol. 30, no. 5, pp. 1161–1182, 2009.
- [18] C. M. Cheng and W. Alpers, "Trapped atmospheric gravity waves over the South China Sea using Envisat synthetic aperture radar images," *Int. J. Remote Sens.*, vol. 31, no. 17–18, pp. 4725–4743, Sep. 2010.
- [19] B. A. Hughes, "The effect of internal waves on surface wind waves—Part 2: Theoretical analysis," *J. Geophys. Res.*, vol. 83, no. C1, pp. 455–465, 1978.
- [20] W. Alpers, "Theory of radar imaging of internal waves," *Nature*, vol. 314, no. 6008, pp. 245–247, Mar. 1985.
- [21] P. Brandt, R. Romeiser, and A. Rubino, "On the determination of characteristics of the interior ocean dynamics from radar signatures of internal solitary waves," *J. Geophys. Res.*, vol. 104, no. C12, pp. 30 039–30 047, Dec. 1999.
- [22] V. Kudryavtsev, D. Akimov, J. A. Johannessen, and B. Chapron, "On radar imaging of current features—Part 1: Model and comparison with observations," *J. Geophys. Res.*, vol. 110, no. C7, p. C07 016, Jul. 2005. DOI:10.1029/2004JC002505.
- [23] W. Alpers and E. Salusti, "Scylla and Charybdis observed from space," *J. Geophys. Res.*, vol. 88, no. C3, pp. 1800–1808, 1983.
- [24] L. Armi and D. M. Farmer, "The internal hydraulics of the Strait of Gibraltar and associated sills and narrows," *Oceanologica Acta*, vol. 8, pp. 37–46, 1985.
- [25] A. Sapia and E. Salusti, "Observation of non-linear internal solitary wave trains at the northern and southern mouths of the Strait of Messina," *Deep-Sea Res.*, vol. 34, no. 7, pp. 1081–1092, Jul. 1987.
- [26] V. Artale, D. Levi, S. Marullo, and R. Santoleri, "Analysis of nonlinear internal waves observed by Landsat thematic mapper," *J. Geophys. Res.*, vol. 95, no. C9, pp. 16 065–16 073, 1990.
- [27] W. Alpers and P. E. La Violette, "Tide-generated nonlinear internal wave packets in the Strait of Gibraltar observed by the synthetic aperture radar on board the ERS-1 satellite," in *Proc. 1st ERS-1 Symp.—Space Service Environ.*, Cannes, France, Nov. 4–6, 1992, pp. 753–758, ESA SP-359.
- [28] C. Richez, "Airborne synthetic aperture radar tracking of internal waves in the Strait of Gibraltar," *Prog. Oceanogr.*, vol. 33, no. 2, pp. 93–97, 1994.
- [29] P. Brandt, W. Alpers, and J. O. Backhaus, "Study of the generation and propagation of internal waves in the Strait of Gibraltar using a numerical model and synthetic aperture radar images of the European ERS 1 satellite," *J. Geophys. Res.*, vol. 101, no. C6, pp. 14 237–14 252, 1996.
- [30] P. Brandt, A. Rubino, W. Alpers, and J. O. Backhaus, "Internal waves in the Strait of Messina studied by a numerical model and synthetic aperture radar images from the ERS 1/2 satellites," *J. Phys. Oceanogr.*, vol. 27, no. 5, pp. 648–663, May 1997.
- [31] R. D. Susanto, L. Mitnik, and Q. Zheng, "Ocean internal waves observed in the Lombok Strait," *Oceanography*, vol. 18, no. 4, pp. 80–87, Dec. 2005.
- [32] A. K. Liu, Y. S. Chang, M.-K. Hsu, and N. K. Liang, "Evolution of nonlinear internal waves in the East and South China Seas," *J. Geophys. Res.*, vol. 103, no. C4, pp. 7995–8008, 1998.
- [33] M. K. Hsu and A. K. Liu, "Nonlinear internal waves in the South China Sea," *Can. J. Remote Sens.*, vol. 26, no. 2, pp. 72–81, 2000.
- [34] W. Huang, J. Johannessen, W. Alpers, J. Yang, and X. Gan, "Spatial and temporal variations of internal wave sea surface signatures in the northern South China Sea studied by spaceborne SAR imagery," in *Proc. SeaSAR*, Frascati, Italy, Jan. 21–25, 2008, pp. 1–6, ESA SP-656.
- [35] J. R. Apel, J. R. Holbrook, J. Tsai, and A. K. Liu, "The Sulu Sea internal soliton experiment," *J. Phys. Oceanogr.*, vol. 15, no. 12, pp. 1625–1651, Dec. 1985.
- [36] K. Zeng and W. Alpers, "Generation of internal solitary waves in the Sulu Sea and their refraction by bottom topography studied by ERS SAR imagery and a numerical model," *Int. J. Remote Sens.*, vol. 25, no. 7/8, pp. 1277–1281, Apr. 2004.
- [37] R. B. Perry and G. R. Schimke, "Large amplitude internal waves observed off the northwest coast of Sumatra," *J. Geophys. Res.*, vol. 70, no. 10, pp. 2319–2324, 1965.
- [38] A. R. Osborne and T. L. Burch, "Internal solitons in the Andaman Sea," *Science*, vol. 208, no. 4443, pp. 451–460, May 1980.
- [39] W. Alpers, H. Wang-Chen, and L. Hock, "Observation of internal waves in the Andaman Sea by ERS SAR," in *Proc. IGARSS*, Singapore, Aug. 3–8, 1997, vol. 4, pp. 1518–1520.
- [40] V. Vlasenko and W. Alpers, "Generation of secondary internal waves by the interaction of an internal solitary wave with an underwater bank," *J. Geophys. Res.*, vol. 110, no. C2, p. C02 019, Feb. 2005. DOI:10.1029/2004JC002467.
- [41] L. Nicolò and E. Salusti, "Field and satellite observations of large amplitude internal tidal wave trains south of the Strait of Messina, Mediterranean Sea," *Ann. Geophys.*, vol. 9, no. 8, pp. 534–539, 1991.
- [42] A. Stoffelen and D. Anderson, "Scatterometer data interpretation: Estimation and validation of the transfer function CMOD4," *J. Geophys. Res.*, vol. 102, no. C3, pp. 5767–5780, 1997.
- [43] Y. Quilfen, B. Chapron, T. Elfouhaily, K. Katsaros, and J. Tournadre, "Observation of tropical cyclones by high-resolution scatterometry," *J. Geophys. Res.*, vol. 103, no. C4, pp. 7767–7786, 1998.
- [44] J. Horstmann, W. Koch, S. Lehner, and W. Rosenthal, "Ocean wind field and their variability derived from SAR," *Earth Obs. Q.*, vol. 59, no. 5, pp. 8–12, 1998.
- [45] F. Monaldo and V. Kerbaol, "The SAR measurement of ocean surface winds: An overview," in *Proc. 2nd Workshop Coastal Marine Appl. SAR*, Svalbard, Norway, Sep. 8–12, 2003, pp. 15–32.

- [46] J. Horstmann and W. Koch, "Comparison of SAR wind field retrieval algorithms to a numerical model utilizing ENVISAT ASAR data," *IEEE J. Ocean. Eng.*, vol. 30, no. 3, pp. 508–515, Jul. 2005.
- [47] J. W. Rottman and F. Einaudi, "Solitary waves in the atmosphere," *J. Atmos. Sci.*, vol. 50, no. 14, pp. 2116–2136, Jul. 1993.
- [48] F. D. Eaton, S. A. McLaughlin, and J. R. Hines, "A new frequency-modulated continuous wave radar for studying planetary boundary layer morphology," *Radio Sci.*, vol. 30, no. 1, pp. 75–88, Jan./Feb. 1995.
- [49] J. D. Doyle and D. R. Durran, "The dynamics of mountain-wave induced rotors," *J. Atmos. Sci.*, vol. 59, no. 2, pp. 186–201, Jan. 2002.
- [50] R. A. Goler and M. J. Reeder, "The generation of the Morning Glory," *J. Atmos. Sci.*, vol. 61, no. 12, pp. 1360–1376, Jun. 2004.
- [51] R. Romeiser and W. Alpers, "An improved composite surface model for the radar backscattering cross section of the ocean surface—Part 2: Model response to surface roughness variations and the radar imaging of underwater bottom topography," *J. Geophys. Res.*, vol. 102, no. C11, pp. 25 251–25 267, Nov. 1997.
- [52] G. R. Valenzuela, "Theories for the interaction of electromagnetic and ocean waves—A review," *Boundary Layer Meteorol.*, vol. 13, no. 1–4, pp. 61–85, Jan. 1978.
- [53] V. Vlasenko, L. Ostrovsky, and K. Hutter, "Adiabatic behavior of strongly nonlinear solitary waves in slope-shelf areas," *J. Geophys. Res.*, vol. 110, no. C4, p. C04 006, Apr. 2005. DOI:10.1029/2004JC002705.
- [54] M. F. Maury, *The Physical Geography of the Sea and Its Meteorology*. New York: Harper, 1861, pp. 404–405.
- [55] Q. Zheng, Y. Yuan, V. Klemas, and X.-H. Yan, "Theoretical expression for an ocean internal soliton SAR image and determination of the soliton characteristic half width," *J. Geophys. Res.*, vol. 106, no. C12, pp. 31 415–31 423, 2001.
- [56] M. J. Curry and R. C. Murty, "Thunderstorm-generated gravity waves," *J. Atmos. Sci.*, vol. 31, no. 5, pp. 1402–1408, Jul. 1974.
- [57] C. O. Erickson and L. F. Whitney, "Picture of the month. Gravity waves following severe thunderstorms," *Mon. Weather Rev.*, vol. 101, no. 9, pp. 708–711, Sep. 1973.
- [58] R. J. Doviak and D. R. Christie, "Thunderstorm generated solitary waves: A wind shear hazard," *J. Aircr.*, vol. 26, no. 5, pp. 423–431, 1989.
- [59] A. J. Prata, P. G. Baines, and P. C. Tildesley, "Observations of concentric ring clouds west of Australia," *Int. J. Remote Sens.*, vol. 22, no. 14, pp. 2847–2852, Sep. 2001.
- [60] C. Melsheimer, W. Alpers, and M. Gade, "Investigation of multifrequency/multipolarization radar signatures of rain cells derived from SIR-C/X-SAR data," *J. Geophys. Res.*, vol. 103, no. C9, pp. 18 867–18 884, 1998.
- [61] I.-I. Lin, W. Alpers, V. Khoo, H. Lim, T. K. Lim, and D. Kasilingam, "An ERS-1 synthetic aperture radar image of a tropical squall line compared with weather radar data," *IEEE Trans. Geosci. Remote Sens.*, vol. 39, no. 5, pp. 937–945, May 2001.
- [62] C. Melsheimer, W. Alpers, and M. Gade, "Simultaneous observations of rain cells over the ocean by the synthetic aperture radar on board the ERS satellites and by surface-based weather radars," *J. Geophys. Res.*, vol. 106, no. C3, pp. 4665–4677, 2001.
- [63] W. Alpers and C. Melsheimer, "Rainfall," in *Synthetic Aperture Radar Marine User's Manual*, C. R. Jackson and J. R. Apel, Eds. Washington, DC: Nat. Ocean. Atmos. Admin., Center Satellite Appl. Res., NOAA/NESDIS, 2004, ch. 17.
- [64] W. Alpers, C. M. Cheng, Y. Shao, and L. Yang, "Study of rain cells over the South China Sea by synergistic use of multi-sensor satellite and ground-based meteorological data," *Photogramm. Eng. Remote Sens.*, vol. 73, no. 3, pp. 267–278, Mar. 2007.
- [65] W. Alpers and I. Hennings, "A theory of the imaging mechanism of underwater bottom topography by real and synthetic aperture radar," *J. Geophys. Res.*, vol. 89, no. C6, pp. 10 529–10 546, Nov. 1984.
- [66] W. Huang and B. Fu, "A spaceborne SAR technique for shallow water bathymetry surveys," *J. Coastal Res.*, no. 43, pp. 223–228, 2004.
- [67] W. Alpers and B. Brümmer, "Atmospheric boundary layer rolls observed by the synthetic aperture radar on board the ERS-1 satellite," *J. Geophys. Res.*, vol. 99, no. C6, pp. 12 613–12 621, Jun. 1994.
- [68] V. Vlasenko, P. Brandt, and A. Rubino, "Structure of large-amplitude internal solitary waves," *J. Phys. Oceanogr.*, vol. 30, no. 9, pp. 2172–2185, Sep. 2000.
- [69] W. Huang, X. Gan, J. Yang, B. Fu, and P. Chen, "Role of surface winds in SAR signatures of oceanic internal waves in the northern South China Sea," in *Proc. SPIE—Remote Sens. Ocean Sea Ice Large Water Regions 2009*, C. R. Bostater, Jr., S. P. Mertikas, X. Neyt, and M. Velez-Reyes, Eds., 2009, vol. 7473, pp. 747 30K–747 30K-5.
- [70] S. Ufermann and R. Romeiser, "A new interpretation of multifrequency/multipolarization radar signatures of the Gulf Stream front," *J. Geophys. Res.*, vol. 104, no. C11, pp. 25 697–25 706, 1999.
- [71] S. Ufermann and R. Romeiser, "Numerical study on signatures of atmospheric convective cells in radar images of the ocean," *J. Geophys. Res.*, vol. 104, no. C11, pp. 25 707–25 720, 1999.
- [72] C. J. Nappo, *An Introduction to Atmospheric Gravity Waves*. New York: Academic, 2002.
- [73] R. S. Scorer, "Theory of waves in the lee of mountains," *Q. J. R. Meteorol. Soc.*, vol. 75, no. 323, pp. 41–56, Jan. 1949.



**Werner Alpers** (M'93–SM'04) received the Diploma in physics from the University of Hamburg, Hamburg, Germany, in 1962, the M.S. degree in physics from the University of Wisconsin-Madison in 1964, and the Ph.D. degree in theoretical physics (elementary particle physics) from the University of Hamburg in 1967.

He was with the European Space Research Institute (ESRIN), Frascati, Italy, from 1968 to 1970 and with the Max-Planck-Institute for Physics and Astrophysics, Institute for Extraterrestrial Physics, Garching, Germany, from 1970 to 1973, where he carried out research in the field of space physics and cosmic ray physics. In 1973, he became engaged in remote sensing of the ocean and worked from 1973 to 1985 with the University of Hamburg and the Max-Planck-Institute for Meteorology, Hamburg. From 1985 to 1989, he was an Associate Professor with the Department of Physics and Electrical Engineering, University of Bremen, Bremen, Germany, and from 1989 until his retirement in 2001, he was a Full Professor with the Institute of Oceanography, University of Hamburg, where he established the research group "Satellite Oceanography." From 1998 to 2001, he was also the Managing Director of the Institute of Oceanography, University of Hamburg. Since 1973, he has been engaged in microwave remote sensing of the ocean by using laboratory, airborne, and spaceborne sensors, as well as theoretical models. He has authored or coauthored more than 110 papers in peer-reviewed journals and books dealing with different aspects of microwave remote sensing of the ocean. After his retirement, he has continued carrying out research in the field of satellite oceanography at the University of Hamburg, in collaboration with scientists from several foreign countries, in particular from China. Furthermore, he has given many lectures in ESA-sponsored training courses dealing with remote sensing of the ocean.

Dr. Alpers was the General Chairman of the 1999 IEEE Geoscience and Remote Sensing Symposium (IGARSS'99), Hamburg, Germany. He was active in several advisory committees of the German Ministry of Science and Technology, the German Science Foundation, the European Science Foundation, and the European Space Agency (ESA) for defining Earth observation satellite missions. In particular, he was involved from the beginning in the ERS-1, ERS-2, and Envisat satellite projects as a Scientific Advisor to ESA.



**Weigen Huang** received the Ph.D. degree in marine remote sensing from Dundee University, Dundee, U.K., in 1990.

During the period of 1990–1992, he was a Research Fellow with the Department of Oceanography, University of Southampton, Southampton, U.K., and was continuing on research in marine remote sensing. Since September 1992, he has been with the Second Institute of Oceanography (SIO), State Oceanic Administration (SOA), Hangzhou, China. He is currently the Director of the Centre for Marine Remote Sensing and Numerical Modeling, the Deputy Director of the State Key Laboratory of Satellite Ocean Environment Dynamics (SOED), and a Principal Research Scientist with SIO, SOA. He currently serves on the Editorial Board of four academic journals, including the *International Journal of Remote Sensing*. He has undertaken research in microwave remote sensing of the ocean and satellite oceanography. In addition to his research duties, he teaches marine remote sensing technique and applications at SIO and the Ocean University of China, Qingdao, China. He has published about 200 papers.